Marine and Petroleum Geology 122 (2020) 104614

Contents lists available at ScienceDirect

Marine and Petroleum Geology

journal homepage: www.elsevier.com/locate/marpetgeo

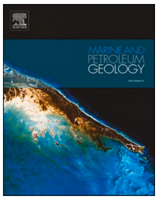

Research paper

Pore network analysis of Brae Formation sandstone, North Sea

Paul-Ross Thomson [a,*], Mark Jefferd [b], Brett L Clark [c], Domenico Chiarella [a], Thomas M Mitchell [b], Saswata Hier-Majumder [a]

[a] Department of Earth Sciences, Royal Holloway University of London, Egham, Surrey, TW20 0EX, UK
[b] Department of Earth Sciences, University College London, UK
[c] Natural History Museum, London, UK

ARTICLE INFO

Keywords:
Digital rock physics
Porosity
Permeability
Pore network model
Reservoir
X-ray micro-CT
Brae formation
Miller field

ABSTRACT

In this work, we apply digital rock physics (DRP) to characterize the pore networks of the Brae Formation sandstones from two different wells in the Miller field area (North Sea, UK). Using X-ray micro-CT scans, we calculate the porosity and permeability and generate pore network models to assess pore shape characteristics. The porous samples are marked by macroporosities ranging from 4.9% to 15.2% with the effective porosities varying from 0 to 14.8%. The samples also contained some microporosity hosted in secondary and accessory mineral phases, varying between 2.6% and 10.7%. Pore network model results for total porosity indicate that the samples have median pore and throat radii ranging from 5.5 μm to 16.8 μm and 6.4 μm–12.9 μm, respectively. The throat length of all samples has a median value ranging between 36.3 μm and 82.4 μm. The ratio between effective porosity and total porosity (φ^*) varies with total porosity (φ) following the exponential relation $\varphi^* = 0.98 - e^{-(\varphi-0.032)/0.028}$. Pore network connectivity is established at a porosity of 3% and full communication is achieved at porosities exceeding 10%. Permeability was found to vary with total porosity with an exponent of 3.67. Based on these observations and the results from our models, the connectivity of the pore network has important implications for predicting reservoir performance during large scale subsurface projects such as hydrocarbon production and CO_2 storage.

1. Introduction

Generating an accurate reservoir model is of critical importance in forecasting the lifespan of hydrocarbon reservoirs and estimating the efficiency of carbon capture and sequestration. One critical parameter controlling the flow of fluids within subsurface reservoirs is the fraction of effective or connected pore spaces in the reservoir. Effective porosity, the primary conduit of porous flow, can be significantly smaller than the bulk porosity of the rock determined from well logs. In reservoir rocks, especially those containing clay minerals and accessory phases, a significant part of the pore space can be trapped in micropores which are unfavorable to porous flow (Thomson et al., 2019; Bultreys et al., 2016). Additionally, effective porosity within the macropores—pores distributed along grain edges and corners—can be significantly lower than the total macroporosity. To quantify the connectivity of the pore space, it is therefore necessary to combine high resolution visualization of pore spaces with bulk measurements.

In this work, we address the issue of quantifying effective pore space in a well studied suite of natural sandstones from a former producing hydrocarbon field in the North Sea. Using digital rock physics (DRP) techniques, we compare the pore network characteristics of the Brae Formation sandstones occurring at different depth intervals. The Brae Formation comprises primary reservoir rock in the Miller Oil Field, located at the western edge of the South Viking Graben (Rooksby, 1991). These rocks have been studied extensively in the context of hydrocarbon exploration and carbon capture and sequestration (Lu et al., 2011; Maast et al., 2011; Rooksby, 1991).

The Southern Viking Graben is an Upper Jurassic rift basin containing a major hydrocarbon province extending over the geographic border separating United Kingdom and Norway (Fig. 1A; Turner and Cronin (2018)). In particular, a large proportion of hydrocarbon reserves is contained in synrift deposits, which constitute the Brae Formation. The Kimmeridgian-Tithonian Brae Formation consists of the Brae 1 and Brae 2 zones representing the result of large volumes of clastic material that were sourced from the Fladen Ground Spur area into the South Viking Graben (Fig. 1B). Deposits result in unsteady

---

* Corresponding author.
E-mail address: paul-ross.thomson.2016@live.rhul.ac.uk (P.-R. Thomson).

https://doi.org/10.1016/j.marpetgeo.2020.104614
Received 27 July 2019; Received in revised form 2 March 2020; Accepted 23 July 2020
Available online 22 August 2020

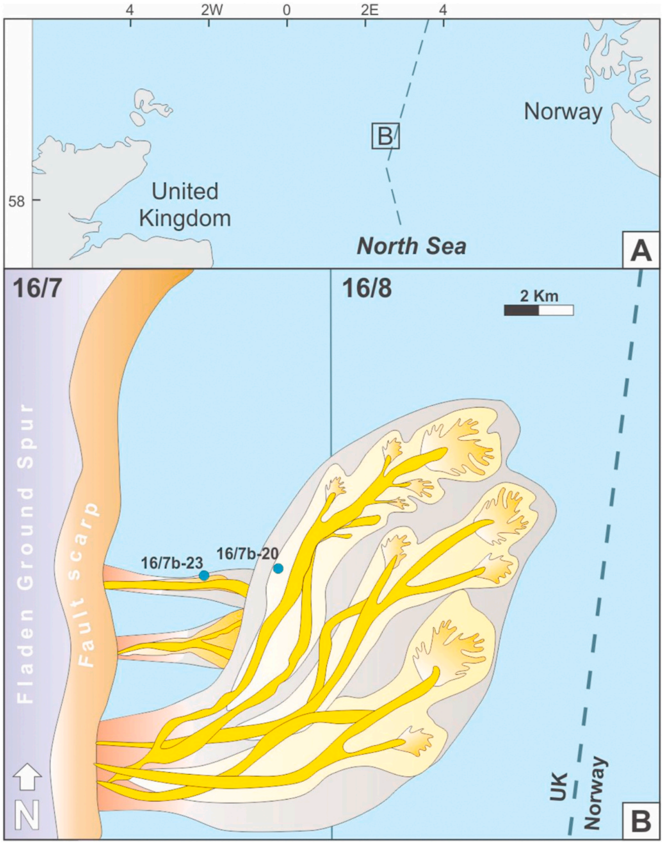

Fig. 1. (A) Map of the North Sea showing the position of the studied system. (B) Depositional map of the Miller Fan system (Brae Formation) with the position of the studied pair of cored wells.

fault-controlled systems evolving into stready-state phases (sensu Chiarella et al., 2020 (in press)) fed through sand-rich turbiditic flows forming vertically- and laterally-stacked lobe elements (McClure and Brown, 1992). The Brae sandstone reservoirs are encased and distally interfingered within the organic-rich hemipelagic shale of the Kimmeridgian Clay Formation (Rooksby, 1991). In this study, we focus on cores recovered from two wells, one from the Miller field (16/7b-20) and the other from the edge of the Central Brae field (16/7b-23), within the depth range between 4040 m and 4064 m. The two cored wells are from different locations within the turbidite fan system in the Brae-Miller field complex. Well 16/7b-23 is located proximal to the sediment source supply and major fault of the South Viking Graben, while well 16/7b-20 is distally located, nearer the center of the graben.

Previous studies on the reservoir characteristics of the South Viking Graben involved porosity derived from well logs (Maast et al., 2011; Rooksby, 1991) and studies of secondary mineral precipitation (Aase and Walderhaug, 2005; Lu et al., 2011; Marchand et al., 2001). These studies indicate that the bulk porosity at depths greater than 4000 m varies widely between 5% and 25% (Maast et al., 2011), with an average bulk porosity of 16% in the Brae Formation (Rooksby, 1991). Studies on the nature of secondary mineralization indicate that the pore space in the sandstone can be filled with varying amounts of clay, microquartz, or carbonate phases (Aase and Walderhaug, 2005; Lu et al., 2011; Maast et al., 2011; Marchand et al., 2001). Despite this array of studies on the nature of the Brae Formation rocks, the nature of connectivity of the pore spaces, values of pore and throat diameters, and the fraction of pore space trapped in the secondary mineral phases remain poorly understood. Quantifying the factors controlling the connectivity of the macropores is crucial in estimating the permeability of the rock.

A number of empirical studies highlight the importance of effective porosity on permeability of reservoir rocks (Gomez et al., 2010; Mavko; Nur, 1997; Revil et al., 2014). The relationship between porosity, φ, and permeability, k, is commonly expressed within the Kozeny-Carman relation of the form $k \propto \varphi^3$, which arises from a model of pores and throats situated along grain corners and edges. Experimental measurements of permeability by Bourbié and Zinszner (1985) demonstrated that this model breaks down at low porosities, typically $< 9 - 10\%$. Mavko and Nur (1997) suggested a modified form of the relation, $k \propto (\varphi - \varphi_p)^3$, where $\varphi_p = 2.5\%$ is defined as the percolation threshold, to address the change in porosity exponent. A number of experimental measurements of permeability in various clean sandstones led to a number of different values of the porosity exponent and the percolation threshold (Doyen, 1988; Madonna et al., 2013; Gomez et al., 2010; Revil et al., 2014). Simultaneous determination of effective porosity and permeability in sandstones allows us to identify the role of pore network connectivity on permeability directly. Despite a number of measurements of bulk porosity and permeability on the Brae Formation sandstone, direct constraints on the permeability arising from an analysis of the pore network still remains poorly understood.

This work aims to bridge this gap by studying the characteristics of the pore network and simulating porous flow in the Brae Formation from high resolution computed microtomographic (micro-CT) volumes. In order to assess microporosity in secondary minerals and clay minerals, we compare our results with bulk porosity measurements using Helium pycnometry. Through X-ray micro-CT techniques, this study aims to characterize the pore volume properties of the Miller field (Brae Formation, Upper Jurassic, North Sea) cored in wells 16/7b-20 and 16/7b-23. Using a pore network model (PNM) approach to quantitatively classify pore space properties of each sample in terms of pore radius, throat radius, throat length and coordination number (number of throats connected to each pore).

2. Materials and methods

We prepared eight different samples for X-ray micro-CT image acquisition by creating 5 mm diameter core plugs. The acquired images were processed to segment the pore volume in each sample. The stacked images produced a 3D pore volume from which the total and effective porosity was measured. These 3D pore volumes were used further to measure the geometry of the pores and throats and to calculate the absolute permeability of each sample. In the following subsections, we outline the details of each of these steps.

2.1. *X-ray micro-CT image acquisition*

To acquire the micro-CT images, cylindrical shaped core samples were prepared. We used eight core samples from British Petroleum, collected within an interval of ~5 m in well 16/7b-20 (between 4040.10 m and 4045.13 m depths) and ~4 m in well 16/7b-23 (between 4061 m and 4063.75 m depths). The 5 mm diameter core plugs used for micro-CT acquisition were drilled from sections of these 15 cm diameter cores. The diameter of the cylinders minimized X-ray absorption by additional sample mass outside the ~4 mm diameter imaging volume. All 8 Brae Formation sandstone samples were labeled according to their depth (BFS1 to BFS8, see also Table 1) and marked to show orientation (way up) from which it had been sampled. Supplementary Fig. S1 shows an example of the original core and one of the ~5 mm core plugs used during image acquisition.

We acquired the X-ray images on a Zeiss Xradia Versa 520 scanner at the Imaging and Analysis Center at The London Natural History Museum. The hardware utilizes a transmission source generating polychromatic X-rays with an energy range between 30 and 160 kV and a maximum power capability of 10 W. The X-ray tube generates a focal spot size, which is small enough to provide sufficient spatial coherence to utilize phase contrast enhancement. Increasing the sample-detector distance to 14 mm allows to detect interference fringes at object

Table 1
Summary of sample data used in this study, including sample name, well ID depth interval, and voxel resolution.

Sample	Well ID	Depth (m)	Macroporosity (Effective)%	Microporosity%	Permeability (mD)
BFS1[a]	16/7b-20	4040.10	7.2±0.4 (5.8)	10.4 ± 1.4	91.2
BFS2[a]	16/7b-20	4041.35	7.1±3.2 (5.7)	8.3 ± 0.3	86.3
BFS3[b]	16/7b-20	4043.75	8.0±0.2 (6.4)	10.2 ± 1.7	7.6
BFS4[b]	16/7b-20	4045.13	9.6±1.0 (9.1)	7.7 ± 2.3	104.2
BFS5[b]	16/7b-23	4061	7.8± 0.5 (5.1)	10.7 ± 1.0	6.7
BFS6[a]	16/7b-23	4062	4.9± 0.6 (0.0)	7.2 ±0.6	0.0*
BFS7[b]	16/7b-23	4063	0.0	2.6 ± 0.7	0.0*
BFS8[a]	16/7b-23	4063.75	15.2 ± 2.0 (14.8)	3.5 ± 0.2	795.1

*Zero effective porosity.
[a] Voxel size 3.9 μm^3.
[b] Voxel size 2.0 μm^3.

boundaries in the images, including mineral phase boundaries inside the rock. Depending on the rock type (composition and grain size) a voltage of 80–100 kV was selected to optimize X-ray transmission. A full 360° rotation was used to collect 3201 projections for each scan to minimize reconstruction artifacts. A camera binning of 2 × 2 was applied to samples requiring higher voltage during the acquisition in order to increase the signal-to-noise ratio and improve overall contrast. Depending on the nature of the sample, we acquired images of resolution 2 μm^3 voxels and 3.9 μm^3 voxels. The image resolution for each sample is reported in Table 1. Data reconstruction was performed using the Zeiss Reconstructor Scout-and-Scan software. A filtered back projection algorithm with beam hardening correction was used to reconstruct the projections to produce a stack of 16-bit tiff images. In the next step, we processed each stack of gray scale images. The micrographs in Fig. 2 show slices of raw gray scale images from each sample.

2.2. Filtering and segmentation

We carried out the image analysis and simulations using the software PerGeos - Thermo Fisher Scientific. The raw gray scale images (e.g. Fig. 3 (a)) are filtered to reduce noise, to smooth the image pixels, and to increase the contrast between pore space, quartz grains and other phases. The non-local means filter (Buades et al., 2008, 2010) was applied to all images. Fig. 3(b) highlights the results of the non-local means filter, with enhanced image quality and no apparent loss of microstructural detail. The 3D images used in this study were largely free from artifacts such as beam hardening and bright fringes along mineral grains (Thomson et al., 2018), therefore, no special filtering was necessary.

The filtered images were segmented to separate macropores from other phases, such as quartz, feldspar, carbonates, and clays (Ketcham and Carlson, 2001; Wildenschild et al., 2002; Iassonov et al., 2009). All the samples used in this study contained variable amounts of microporosity, associated with micron to submicron sized pore spaces, and are included in secondary mineral growths and clay minerals. The dimension of these micropores are beyond the resolution of the scanner, precluding a quantitative estimate of microporosity based on the microtomographic images (Thomson et al., 2019). As a result, we employed a binary segmentation technique. In this method, we segment the images into two phases: macropores and solids. Fig. 3(c) shows a 2D slice following the binary segmentation of the macroporosity phase (blue). The macroporosity consists of both pores and throats, with pores located at grain corners acting as a junction between two or more throats that form along the edge of grains. Solids comprise of all mineral grains as well as parts of the matrix containing microporosity. We carried out the pore network modeling in the macropores, while the volume fraction of micropores were determined by the use of Helium pycnometry

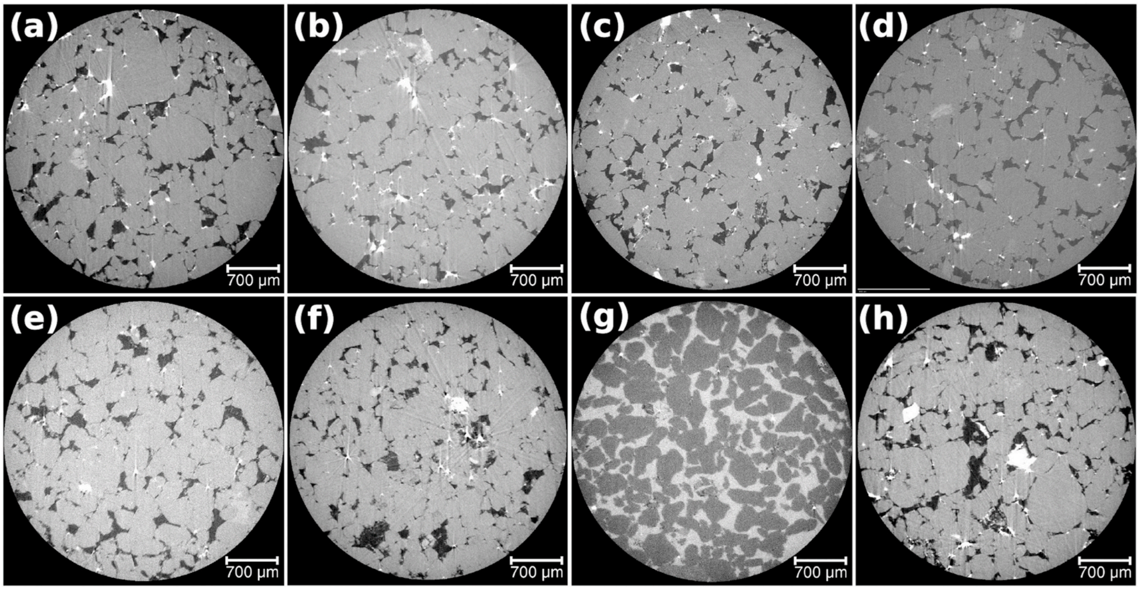

Fig. 2. Gray scale image slices of the eight samples studied in this work. The panels are arranged numerically from samples BFS1 (a) to BFS8 (h). The scale bar in each image represents 700 µm. Resolution of the images in voxel size are reported in Table 1.

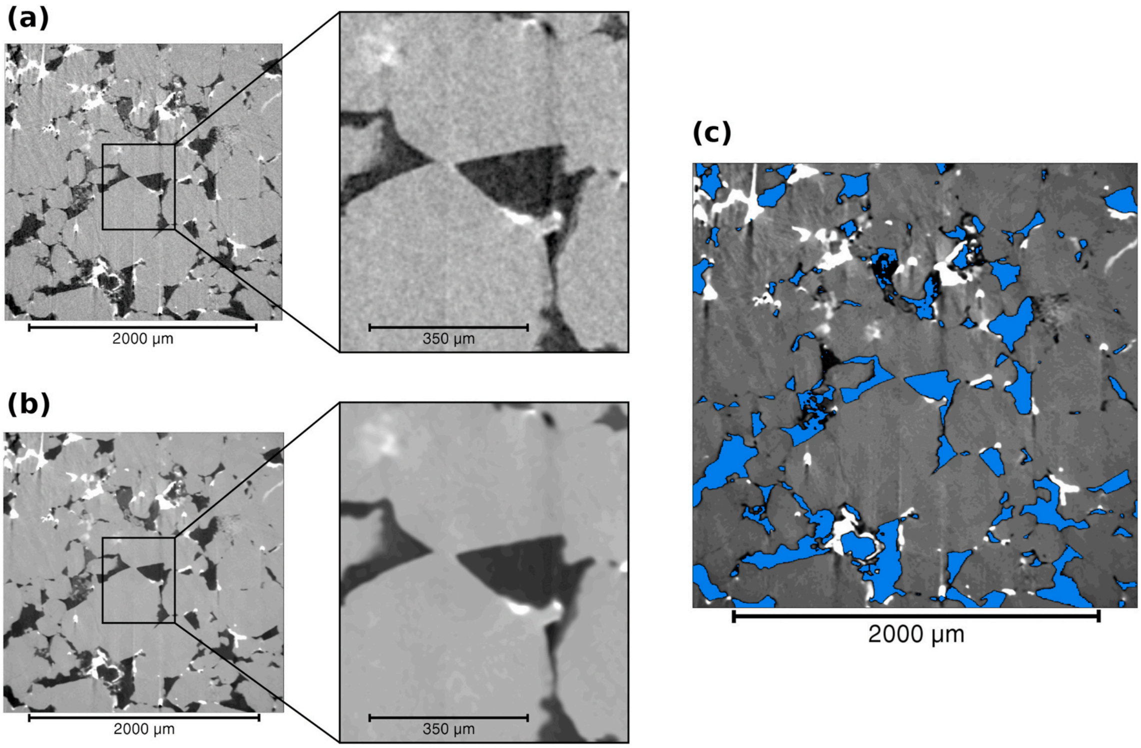

Fig. 3. Image processing steps: (a) 2D slice of the raw image data with zoomed inset showing speckled pixelated texture, (b) 2D slice following non-local means filter with zoomed inset showing smoothed pore and grain texture, and (c) 2D image showing segmentation of the macropore phase (blue). (For interpretation of the references to color in this figure legend, the reader is referred to the Web version of this article.)

measurements.

In the binary segmentation method, we selected the two phases using both an automated segmentation technique (Otsu, 1979) and a manual interactive thresholding selecting the peaks on the bimodal histogram of gray scale intensity. The phases are defined based upon their gray scale color, which is a function of X-ray attenuation, related to the density of different materials in the samples. Fig. 4(a) shows a 3D volume rendering visualization of the filtered raw data, highlighting a very dark gray/black shade that belongs to the macropore space; the micropores were marked by specular patches of dark gray, surrounded by a lighter gray; while quartz grains and other minerals such as carbonates and clay minerals are associated with lighter shades of gray, forming a broad peak at the higher intensity end of the spectrum. For the threshold segmentation of the macropores, we assigned pixels from the peak at the low intensity end of the gray scale histogram. All samples have pixel intensity values between a range of 0 and 6200 for the macroporosity. A number of previous studies explored the relative merits of automated global segmentation and local segmentation methods (Iassonov et al., 2009; Pal and Pal, 1993; Sezgin; Sankur, 2004; Trier and Jain, 1995) While an automated thresholding algorithm circumvents the possibility of operator bias, this method can neglect local variations in gray scale intensity, leading to over or underestimation of macroporosity (see Thomson et al., 2019, and references therein). While we calculated the porosity using both techniques, we found that the automated thresholding method consistently led to inaccurate phase boundary detection when compared with the original gray scale images. We report the macroporosity calculated using both techniques in Table 1 in the supplement, but in the main article and subsequent calculations, we use our

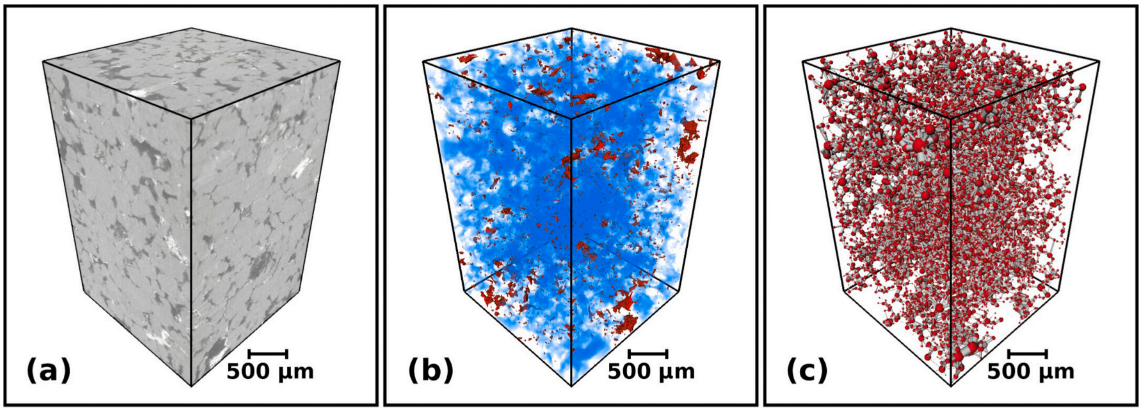

Fig. 4. Raw image and pore network model output from sample BFS8. (a) A 600 × 600 × 900 voxels 3D stack of gray scale images. (b) Volume rendering of effective porosity (blue) and unconnected pore spaces (red). (c) Pore network model of total porosity, scaled to show pore radius and throat radius, where red spheres represent pores and gray cylinders are throats. This sample contains a total porosity of 15.2 vol% and an effective porosity of 14.8 vol%. Scale bar = 500 μm. (For interpretation of the references to color in this figure legend, the reader is referred to the Web version of this article.)

preferred results from manual thresholding. To ensure that the macropores were represented accurately, pixels assigned to the macropore phase were checked visually at various intervals in the samples (e.g. top, middle, bottom). We used this process to check that the pixels selected as part of the macroporosity network were consistent throughout the sample and to avoid the unwanted inclusion of pixels from other materials.

2.3. Pore network modeling and microporosity

The first step in pore network modeling is the determination of total macroporosity. We use the macropore space from the binary segmented images to evaluate total macroporosity. To quantify the uncertainty in the total macroporosity in each sample, we evaluated the total macroporosity over a number of regions of interest (ROI) of different dimensions. We then take the maximum variation in the calculated macroporosity and report this variation as the uncertainty. All porosity measurements and the dimensions of their ROIs are reported in Table 1 of the supplement. Once the total macroporosity was evaluated, we then quantified the effective macropore space.

We used the segmented gray scale images to quantify the macropore network characteristics, and to evaluate the permeability through numerical simulations. To provide the most representative data, samples were cropped to volumes just below that of their maximum dimensions. For samples acquired with voxels dimensions of 2.0 μm^3, we specified a ROI of dimension 600 × 600 × 900 voxels. The samples acquired at lower resolutions of 3.9 μm^3 had ROIs of 1200 × 1200 × 1800 voxels. As discussed earlier, in this study the focus of our digital rock physics analysis is entirely on the macroporosity of the sandstone samples.

In order to characterize the geometry of the pore volume, the 3D segmented label fields must be processed by a skeletonization algorithm (See Thomson et al. (2018, 2019) for additional information about the algorithm). The pore network model extension in PerGeos uses a hybrid algorithm (Youssef et al., 2007) to erode the 3D pore geometry into a one voxel thick skeleton. The skeleton retains the original geometry of the pore network and is used to calculate the length and connectivity of each line. Throats are identified as the one voxel thick lines on the skeleton, while pores are defined as the junctions where two or more throats intersect. The number of throats intersecting a pore is defined as the coordination number of the pore. Pores and throats are designated based on a known extreme radius and their dimensions are calculated based on the expansion of a sphere within pores and the length and equivalent hydraulic radius in each throat. Results of the algorithm include both numerical data (e.g. coordination number, pore radius, throat radius, and throat length) and 3D volumes (node and branch representations).

The pore network model was used to measure the pore geometries for both total porosity and effective (connected) porosity. The volume fraction of total porosity was calculated by combining each voxel assigned to the pore space to produce a 3D volume. To calculate the effective porosity, the total pore space was further processed to determine a percolation threshold. If a network of pores connects at least one pair of opposing faces of the 3D volume, then the network is classified as effective. Pores made up of voxels that do not contribute to the effective network are classified as isolated and are filtered as a consequence of the axis connectivity algorithm. Once the pores and throats involved in the connected network are identified, the effective porosity is calculated based on their representative voxels. Fig. 4(b) shows a 3D volume rendering visualization of the effective pore network (blue) and isolated pores (red) in sample BFS8. Fig. 4(c) shows a pore network model representation of the total porosity found in sample BFS8. In this idealized model, the pores are shown as red spheres, while throats are displayed as gray cylinders. These models can provide useful visual aids to compare and contrast the frequency of large pores and throats in each sample.

In order to account for microporosity in the samples, we carried out bulk porosity measurements using Helium pycnometry. We used two sets of samples to carry out these measurements. In the first set of measurements, we used the cylindrical samples that were used to obtain the micro-CT images. In the second set, we prepared larger cylinders of the rocks from the same core. Details of the Helium porosity measurements are provided in the supplementary material. Since the Helium pycnometer measures both the effective micro and macroporosity, we calculated the microporosity by subtracting the macroporosity from the Helium pycnometry measurements.

2.4. Permeability simulations

The 3D images for the effective pore network were used to assess the absolute permeability in each sample. Since these are the only pores considered to contribute to flow, the isolated pores that do not form part of the effective 3D network are ignored. A finite volume solver (from the petrophysics module in PerGeos) was used to calculate the flow of water through the effective pore space. The equations for mass and momentum conservation for the fluid flow are

$$\nabla \cdot \boldsymbol{u} = 0, \tag{1}$$

$$-\nabla P + \mu \nabla^2 \boldsymbol{u} = 0, \tag{2}$$

where $\boldsymbol{u}$ is the fluid velocity vector, P is the pressure and μ is the viscosity of water ($= 1 \times 10^{-3}$ Pa s). The boundary conditions for the simulation are described in detail by Thomson et al. (2018). We used an iterative solver to determine the velocity and pressure. The iterations were continued until the L_2 norm of the residuals reached a predetermined tolerance level. As shown by Thomson et al. (2019) the tolerance level for error, ε, strongly determines the numerical value of permeability obtained from the simulations. Using a predetermined value for $\varepsilon \leq 10^{-6}$ the permeability is measured and compared between all samples with an effective pore network.

3. Results

The results of porosity and permeability analysis from our images are displayed graphically in Fig. 8. Additional detailed information on the porosity and permeability is provided by quantitative analysis in Section 3.1. The results from porosity, pore network modeling and permeability image analysis are summarized in Table 1 of the supplementary material. The results of the pore network modeling are described in Section 3.2.

3.1. Total and effective porosity

The total porosity is given by the inclusion of effective and isolated pores in the samples that were analyzed. All but one of the samples has visual porosity, which, based on our methods, provided measurements for total and effective pore networks in most samples. Sample BFS7 was the only rock type that appears cemented and does not show clear pore spaces (Fig. 2(g)). Across the two cored wells, measured porosity ranged from 4.9% to 15.2%.

The samples from well 16/7b-20 range in total macroporosity from 7.1% to 9.6%, with a mean value of 8.0%. Effective porosity values range from 5.7% to 9.1%, with a mean value of 6.8%. Within the narrow range of depth in our dataset, no distinct correlation between porosity and depth was observed. As indicated in Table 1, the average bulk porosity (macro and micro combined) in this well is 17%. This value is in good agreement with the 16% bulk porosity estimated by Rooksby (1991). The samples acquired from well 16/7b-23 have total porosity ranging from 4.9% to 15.2%, with a mean value of 9.3%. The pore space in one of the samples from this well, BFS7, was completely replaced by carbonate precipitates (see Fig. 2(g)). In another sample, BFS6, the macroporosity was 4.9%, without a detectable effective network. Fig. S2 within the supplementary material shows the volume rendering

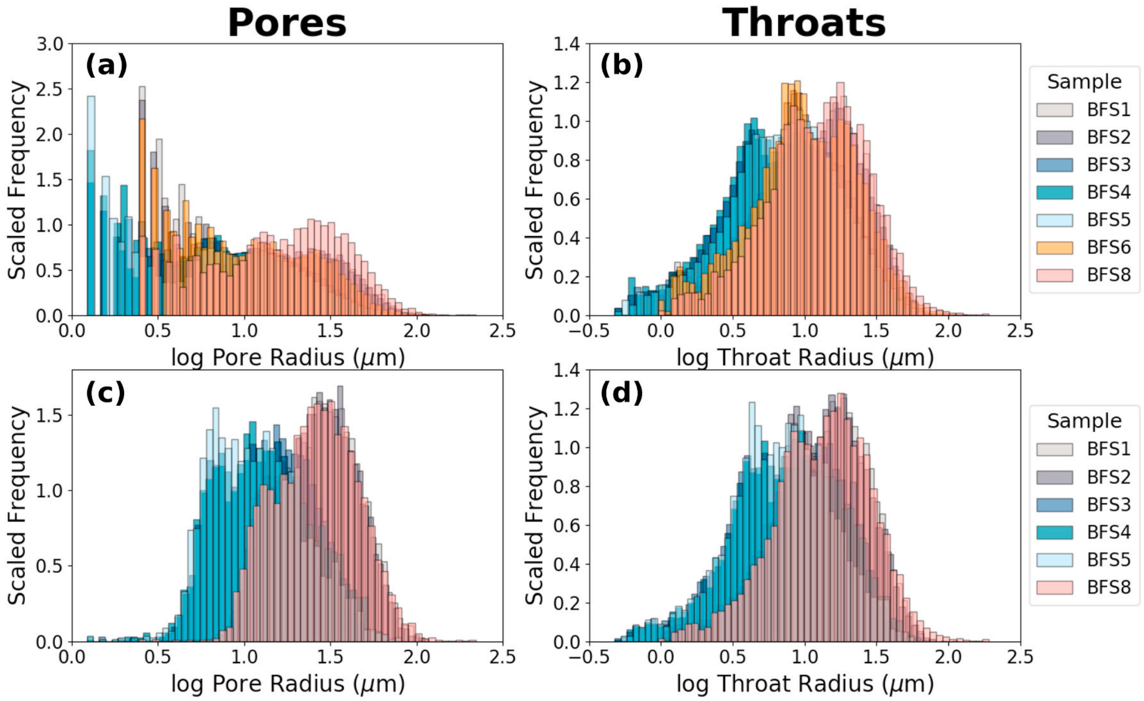

Fig. 5. Log normal distribution of pore and throat geometries in the total pore network ((a) and (b)) and effective pore network ((c) and (d)). The left column illustrates the distribution of pore radii, while the right column displays the distribution of throat radii. The histograms have been normalized to emphasize the distinction between them.

visualization for all samples with a pore network, including sample BFS6 (f) with no connected, effective pore space. As a result, these two samples were unusable for permeability simulations. Of the two samples that have an effective network of pores, their volume fractions are 5.1% and 14.8%, with a mean value of 12.6%. These measurements were performed on the largest ROI to give the most representative data possible. Much like the analysis in the previous well, we do not observe any particular trend in porosity with increasing depth.

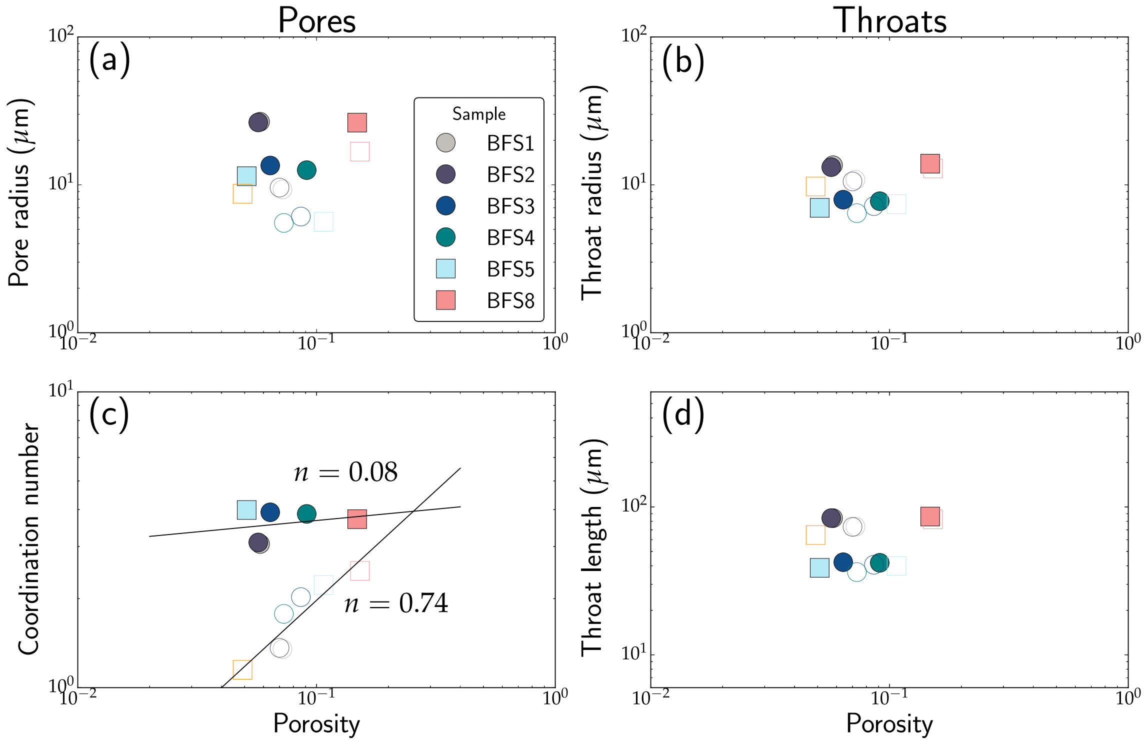

Fig. 6. Pore geometry characteristics for the seven samples in this study. The panels display log-log plots of (a) pore radius, (b) throat radius, (c) mean coordination number, and (d) throat length as a function of total porosity. Core-derived data from wells 16/7b-20 and 16/7b-23 are symbolized by circles and squares, respectively. Filled symbols represent data that display effective porosity while open symbols indicate data that make up total porosity.

3.2. Pore network modeling

Output from the pore network models reveal a number of distinct features of total and effective macroporosities. First, we compare the distribution of pore and throat radii in the total porosity and effective porosity. The histograms in Fig. 5 compare the histograms of logarithmic pore and throat radii in total porosity (panels (a) and (b)) with those in effective porosity. The pore radius of the total pore space in all samples show a peak near the low end in Fig. 5(a). This peak, consisting of small pores, disappears in the distribution of effective porosity. Comparison of the two distributions suggests that the total macroporosity consists of a large number of small, unconnected pores, while the effective pore network consists of fewer, larger pores. The throat radii of the total pore space in Fig. 5(b) and effective pore space in panel (d) both display bimodality. Neither distribution contains a large peak at the low values. Unlike the pore radii, the peaks of throat radii do not show a significant shift to the high values from total to effective porosity. We present the median values of the pore and throat radii, throat lengths, and coordination numbers for all samples in Table 1 of the supplementary material.

An increase in porosity results in larger, better connected pores and throats with considerable variations in the pore network characteristics. The nature of the variation, however, is different between total and effective porosity. In Fig. 6, we plot these variations in median pore radii (panel a), median throat radii (b), mean coordination number (c), and median throat lengths (d). The data from effective porosity are plotted as filled symbols, while the data from total porosity are plotted as open symbols. The sample names are annotated in the legend. While both data sets in panel (a) show that the pore radius increases with an increase in porosity, the median pore radius for effective pores are larger than the total porosity. Despite this difference, the general trend indicates that more porous rocks are characterized by larger pores. This behavior of the pores is also supported by the trend of mean coordination number with porosity. In total porosity, the mean coordination number shows a 3/4 power law relation with porosity as shown by the slope of the log-log plot in panel (c). This variation is practically absent in effective porosity, with mean coordination numbers varying within the narrow range of 3–4 and a log-log slope of 0.08, indicating that the pores in a effective network must be above a threshold value. In contrast, the median throat radius and length in panels (b) and (d) do not display any significant variations between the two sets of porosities, but show a general trend of increase in value with an increase in porosity.

Taken together, the results indicate that pores, junctions in the network, play a crucial role in the effectiveness of the network. Rocks with higher porosity are characterized by larger pores with higher coordination numbers. The results presented here on coordination number of pores are very similar to previous studies involving image analysis and modeled microstructure (Bernabé et al., 2010; Lindquist et al., 2000; Thomson et al., 2018). Theoretical models and analogue material studies also indicate that mean coordination number or the degree of connectivity of a solid phase increase with the increase in phase volume fraction in the material (van de Lagemaat et al., 2001; Zou et al., 2003; Bertei; Nicolella, 2011; Wimert; Hier-Majumder, 2012). To establish an effective pore network, a coordination number of at least 3 is required. The distinction between total and effective porosities are sharpest at low values of total porosity.

The effectiveness of pore space becomes more obvious when we compare the effective porosity with the total porosity. The plot in Fig. 7 (a) compares the effective porosity and the total porosity from our samples. We also include data from the pore network models of sandstones and limestones by Thomson et al. (2019) for comparison. To aid visualization, we plotted a line with a slope of 1 in the figure. At total porosities exceeding 10%, the effective porosity is nearly the same as the total porosity, as the data points fall on the line with a slope of 1. At lower values of total porosity, the effective porosity drops sharply, along the dashed line shown in the figure. This behavior becomes more prominent when the ratio between effective and total porosity is plotted against the total porosity in Fig. 7(b). As both sets of plots indicate, three distinct regimes can be identified from the plot. Above 10% total porosity, nearly 100% of the porosity is effective. We call it the fully effective regime. Below this threshold, the effective porosity drops sharply with a decrease in the total porosity. This is the regime of a partially effective pore network. With further reduction in porosity, the effective pore fraction eventually becomes zero, leading to the zone of isolated pore spaces. Our results indicate that this value is near a total porosity of 3%, similar to previously published estimates of percolation threshold of 2.0%–2.5% (Gomez et al., 2010; Revil et al., 2014; Mavko; Nur, 1997). The ratio between effective and total porosity, φ^*, can be expressed as a decaying exponential function $\varphi^* = a - e^{-(\varphi - b)/c}$ of total porosity, φ. We overlay a fit of this function to the combined data set in Fig. 7(b) with the values of the parameters a, b, and c displayed on the plot. This function is useful in providing a first-order quantitative evaluation of reservoir quality in tight reservoirs typically marked by low total porosity. These results also outline the importance of pore network modeling in understanding the nature of connectivity of reservoir rocks, results that are not attained by traditional bulk porosity measurements.

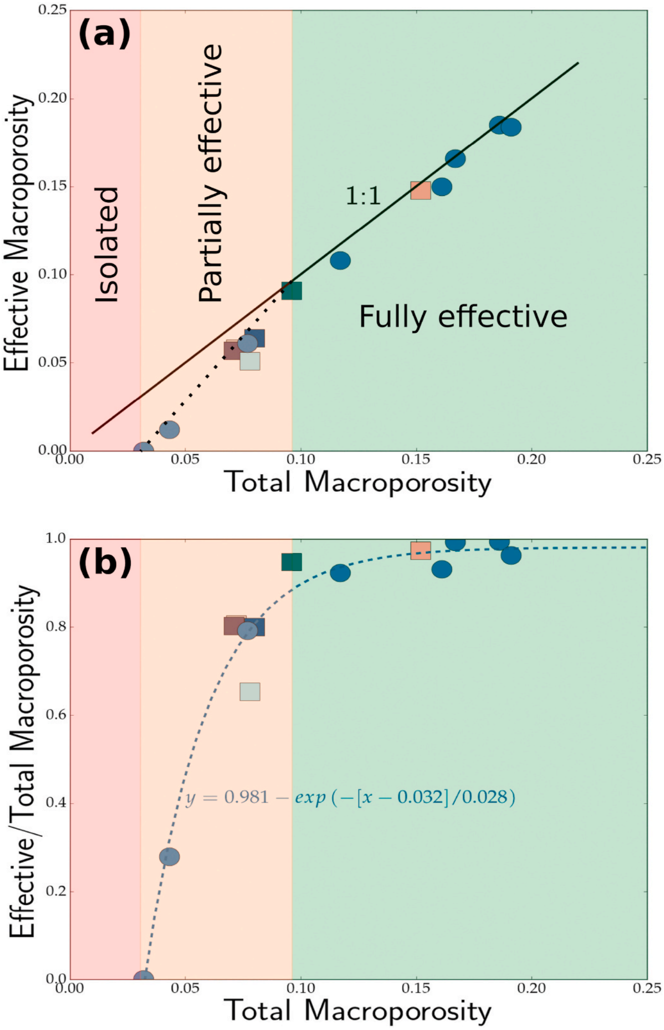

Fig. 7. The effectiveness of pore space in fluid transport. (a) Effective (connected) porosity of the rock as a function of total macroporosity. The solid black line shows the 1:1 correlation. (b) The ratio between effective and total porosity as a function of total porosity. The symbols are the same as in Fig. 8. The dashed blue line is the fit to the data and the equation to the fit is annotated in the plot. (For interpretation of the references to color in this figure legend, the reader is referred to the Web version of this article.)

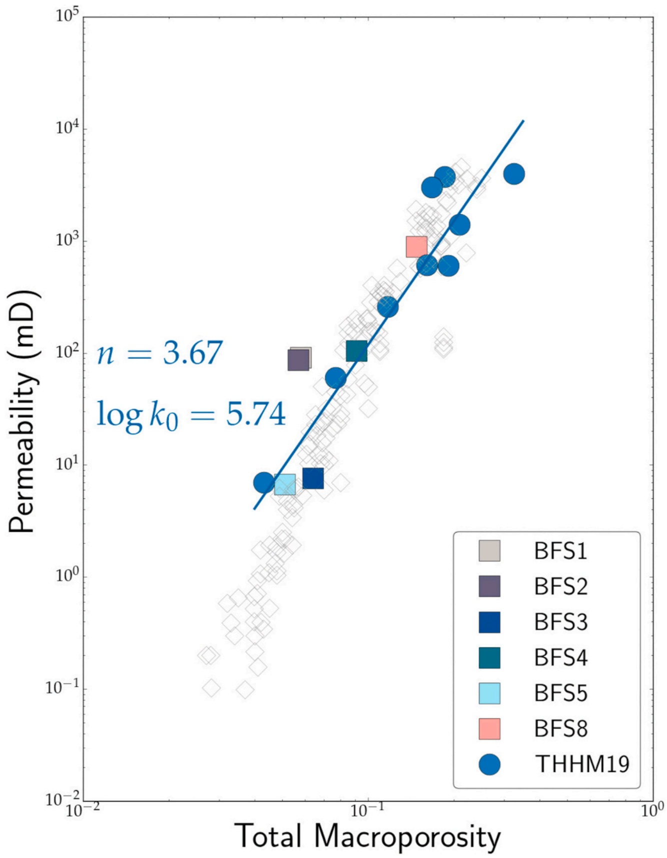

Fig. 8. Plot of permeability as a function of total macroporosity. Square symbols indicate data from the measurements reported in Table 1. For comparison, we also included data points from Thomson et al. (2019), marked as THHM19 in the legends. Open symbols indicate porosity and permeability measurements from laboratory experiments of Doyen (1988); Madonna et al. (2013); Bourbié and Zinszner (1985); Gomez et al. (2010) and Revil et al. (2014). The solid line is a fit to the data with filled symbols of the form $k = k_0\varphi^n$, where k is permeability, measured in mD, k_0 is a constant, φ is total macroporosity, and n is the porosity exponent.

4. Discussion

4.1. Comparison with previous permeability measurements

Effective porosity plays an important role in controlling the permeability of reservoir rocks. A study on experimental determination of permeability of clean Fontainebleau sandstones by Bourbié and Zinszner (1985) demonstrated that the porosity exponent, n, in the Kozeny-Carman relation $k = k_0\varphi^n$ changes from the classical value of 3 to a much higher value of up to 7 as the total porosity decreases below 9%. Citing the role of a percolation threshold, $\varphi_p = 2.5\%$, Mavko and Nur (1997) proposed a modified form of the Kozeny-Carman relation, $k = k_0(\varphi - \varphi_p)^n$, which provided a uniform value of $n = 3$ for the entire range of porosities. Later experimental determinations of permeability showed that this percolation threshold shows some variation between different rock types, but usually varies between 2.0 and 2.5% (Gomez et al., 2010; Revil et al., 2014). In these studies, the percolation threshold was determined by fitting the experimental data. This value, however, is quite similar to the value of ~3% total porosity at which we observe the establishment of a effective pore network in our samples. We also notice that the value of porosity at which the slope of the porosity-permeability curve changes is very close to the value of full connection threshold (8–10%) reported in Fig. 7. Information on pore network connectivity was unavailable for the studies by Bourbié and Zinszner (1985) and Mavko and Nur (1997). The results presented here shows that the two crucial porosity values, the percolation threshold and the slope-break, are associated with the isolation threshold and full connection threshold.

Using the modified Kozeny-Carman relation, Mavko and Nur (1997) obtained a value of the porosity exponent $n = 3$. Later studies by Gomez et al. (2010) and Revil et al. (2014) found that the value of n varies between 4.0 and 4.5 for a percolation threshold of 2%. Another set of experimental measurements of permeability by Doyen (1988) found that using the traditional Kozeny-Carman relation, the porosity exponent is 3.8 over a range of total porosity between 5 and 22%. All of these experiments were carried out in clean sandstones containing negligible amounts of microporosity. Since our macropore network only constitutes of porosity along grain edges and corners, our numerically determined macroporosity and permeability from the Brae Formation sandstone can be directly compared to the raw data from these studies.

In the six samples where we were able to identify an effective porosity, the permeability varied by two orders of magnitude between 7.6 mD and 795.0 mD. We compare the data from the simulations in this study with previous simulation results (e.g. Thomson et al. (2019)) and laboratory experiments (Doyen, 1988; Madonna et al., 2013; Bourbié; Zinszner, 1985; Gomez et al., 2010; Revil et al., 2014) in Fig. 8. In this plot, we overlay a fit of the Kozeny-Carman relation $k = k_0\varphi^n$ to the simulation data from this study and Thomson et al. (2019). The values of the parameters k_0 and n are annotated on the plot. The porosity exponent (n) within the range of our numerical simulations is 3.67, quite similar to the value of 3.8 obtained by Doyen (1988). While the porosity exponents of the modified Kozeny-Carman relation from the study of Gomez et al. (2010) and Revil et al. (2014) are not directly comparable to our fit, we find that the raw data of these studies are largely similar. We also created a fit of permeability as a function of effective porosity, which yielded a slightly lower porosity exponent of 3.3. As discussed earlier, at porosities $< 10\%$, the slope becomes steeper. While the permeability measurements from our models agree quite well with previous empirical data and models, we recognize the fact that empirically determined values of percolation threshold may not reflect the accurate values at which connection is established. Thus, a clearer insight into the nature of porous flow in reservoir rocks can be achieved when permeability measurements are accompanied by pore network models.

4.2. Microporosity

In the North Sea, at depths of greater than roughly 2500 m, quartz and calcite cementation is considered the main porosity-reducing process (Bjørlykke et al., 1992; Giles et al., 1992; Marcussen et al., 2010; Lu et al., 2011). Micro quartz cements range between 3 and 15% while calcite cements range between 0 and 4% in zones that are devoid of calcite concretions and between 20 and 40% in calcite concretion zones (Lu et al., 2011). In addition, the Brae formation sandstones can contain up to 8% clay, muscovite and lithic fragments. These secondary and accessory phases act as sites of microporosity, which can be sampled by bulk porosity measurements but do not participate in fluid percolation.

In agreement with previous studies on the Brae Formation, our samples contain variable amounts of microporosity, typically associated with clay minerals and secondary mineral phases. While a detailed evaluation of the microporosity is outside the scope of this article, we present some Scanning Electron micrographs of several regions of interest in samples BFS1 (a), BFS6 (b), BFS4 (c) and BFS8 (d) in Fig. 9. The images in Fig. 9(a) and (b) show macropore spaces partially filled with microcrystals, rendering the individual pore into a microporous region. The presence of these microcrystals supports previous observation of micro-quartz coating in the Miller field sandstones (Aase and Walderhaug, 2005). Fig. 9(c) and (d) both show the void space filled by a fibrous texture. These micrographs demonstrate the abundance of microporosity in our samples.

One of the key challenges in micro-CT analysis of porous media is the

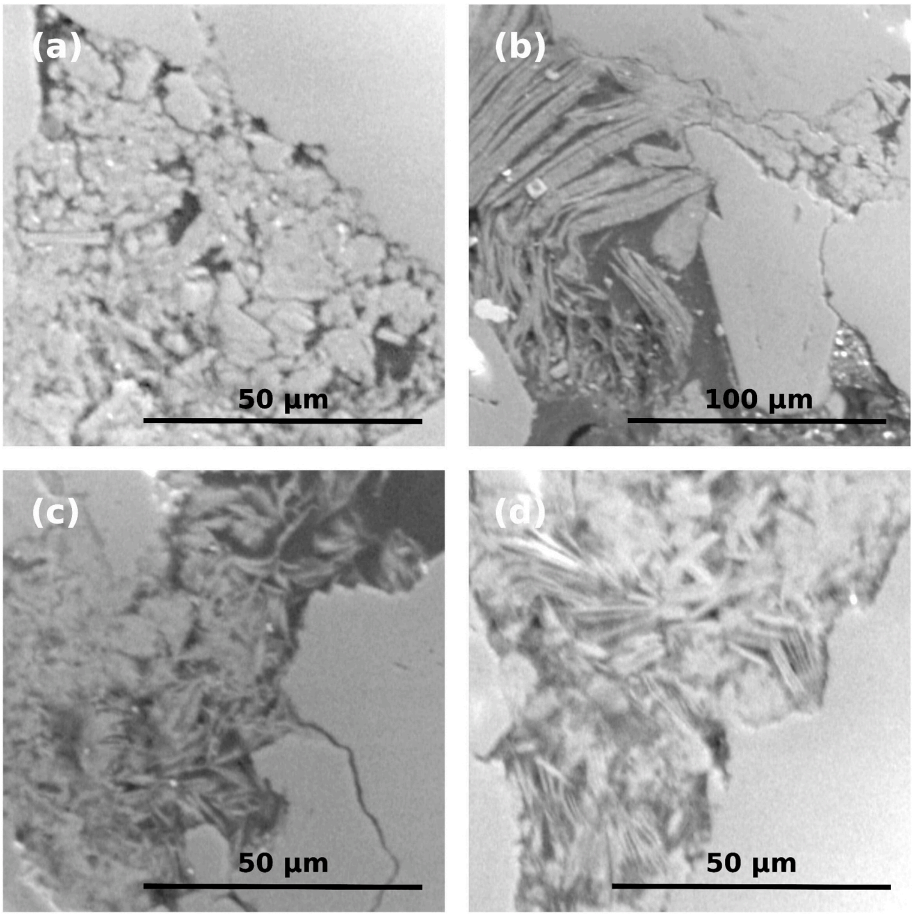

Fig. 9. SEM images showing examples of microporosity below resolution of micro-CT images used in this study. (a) BFS1 with fragmented rock particles and void spaces in between individual grains, (b) BFS 6 showing micro quartz, and fibrous growths in (c) BFS4 and (d) BFS8.

inclusion of microporosity for accurate porosity and permeability measurements. In recent years, several efforts have been made to include porosity at both macro and micro scale using dual-scale models (*e.g.* Mehmani et al. (2019); Mehmani and Prodanović (2014); Bultreys et al. (2016); Soulaine et al. (2016). An alternative approach is to assess the upper and lower limits of the influence of microporous cements on permeability (Thomson et al., 2019). The lower limit, like in this article, considers the micropores as completely impermeable, and fluid flow is only modeled through the macropore network. Since the micropore spaces between microcrystals and fibrous textures are beyond the detection limit of the scanner, we treated these microporous regions as part of the solid matrix during image segmentation. The analysis involving the upper limits considers the micropores as completely void and 100% permeable. While this does not directly quantify the influence of microporosity, it provides a margin of error for permeability measurements using digital methods. The findings of the upper bounds are reported in a forthcoming publication (Thomson et al., 2020). In contrast, low viscosity Helium gas used in Helium pycnometry can penetrate these microporous regions and incorporates the volume of pore space included in the microporosity. As the results from the Helium pycnometry measurements indicate, these samples contain a significant amount of microporosity.

4.3. *Depositional environment and DRP*

The 3D micro-CT image analysis indicates that samples from the core that was recovered from well 16/7b-20 have a more homogeneous internal organization compared to the samples from well 16/7b-23. The reason for such variability in facies and porosity can be attributed to deposition in two different regions within the same depositional area. In particular, the core from well 16/7b-23 penetrates a more proximal area, possibly characterized by higher lateral and vertical facies variability, and moderately sorted sediments. Conversely, although the two wells are located relatively close (~2 km) to each other (Fig. 1B), the core from well 16/7b-20 penetrates an area relatively more distal, sourced from a lateral entry point, and characterized by more mature and well sorted sediments.

This study illustrates variations in macroporosity in a number of sandstone samples at increasing depths across two cored wells in the Miller field complex of the North Sea, South Viking Graben. This area is known for its large regional variation in reservoir quality of deeply buried (> 4000 m) sandstones belonging to the Upper Jurassic syn-rift sequences. Despite these sandstones having similar texture and mineralogy throughout the area, the porosities are known to range between 5% and 25% (Maast et al., 2011). Our porosity measurements fall within this range and we observe some sample intervals with greater porosities and permeabilities occurring at greater depths (e.g. BFS4 and BFS8), while others (e.g. BFS3) are from shallower intervals and display much reduced porosity and permeability.

4.4. *Implications of pore network connectivity*

As the demand for hydrocarbons is expected to continue into the near future and we look to use preexisting reservoirs as potential depositories for CO_2 and other waste products, it is crucial to have a better understanding of pore network connectivity and its control on the rocks ability to store fluid and permit flow. The observations and results of this study indicate the important implications of pore network connectivity for predicting reservoir quality and performance in subsurface formations. Rock formations containing intervals of relatively poor reservoir quality (between 3 and 10% porosity) are undesirable during conventional hydrocarbon production as these can act as baffles to fluid flow, however these may be much more attractive during CO_2 injection, when the goal is for long term storage in the subsurface. On the other hand, formations with good reservoir quality, those with porosity exceeding 10%, will be expected to perform much better during oil and gas production, and can also form more favourable targets for CO_2 storage projects, particularly if the sealing capacity is high and there is low potential for CO_2 to breach and escape the formation. The understanding of pore network connectivity plays an essential role in predicting the reservoir performance of deeply buried rock formations.

While our hypothesis of the three regimes are robust for the scale of resolution of the images, it needs to be further tested. Future work on the relationship between effective porosity and total porosity—determined from multiple resolutions and length scales—will be crucial to determine a number of factors. First, such studies will be able to identify the possible existence of any correlation between the length scales of samples and the boundaries of the three regimes reported above. Second, the existence of such studies will be able to identify the length-independent representative elementary volume (REV) for such samples. Finally, the knowledge of the REV will allow extrapolation and upscaling of these results to reservoir scale simulations.

5. Conclusions

We studied the macropore network characteristics from 8 samples of Brae Formation sandstone from the South Viking Graben in the North Sea. Our results show that the samples contain variable amounts of micro and macroporosity. Our pore network analysis indicates three regimes of pore network connection. At macroporosity values $< 3\%$, the macropore network becomes disconnected, while full connection is achieved at total porosities above 10%. Permeability of the rocks vary between 7.6 and 795.0 mD, with a Kozeny-Carman porosity exponent of 3.67. The pore network connectivity regimes and the permeability results agree well with existing measurements on sandstones.

Credit author statement

Paul-Ross Thomson: Conceptualization, Methodology, Formal Analysis, Investigation, Writing – Original Draft, Writing – Review and Editing, Visualization. **Mark Jefferd:** Helium Pycnometry, Writing – Original Draft. **Brett L Clark:** X-ray CT Image Acquisition, Writing – Original Draft. **Domenico Chiarella:** Sample Collection, Writing – Original Draft, Writing – Review and Editing, Visualization, Supervision. **Tom Mitchell:** Helium Pycnometry, Supervision. **Saswata Hier-Majumder:** Conceptualization, Methodology, Validation, Formal Analysis, Resources, Writing – Original Draft, Writing – Review and Editing, Visualization, Supervision, Project Administration, Funding Acquisition.

Declaration of competing interest

The authors declare that they have no known competing financial interests or personal relationships that could have appeared to influence the work reported in this paper.

Acknowledgments

P-RT acknowledges support from a NERC Oil and Gas CDT graduate fellowship (grant number NE/M00578X/1). MJ acknowledges support from a DTP grant (UK Natural Environment Research Council, NE/L002485/1). This research was also supported by the grant EAR125880 from the US National Science Foundation. DC acknowledges support from AkerBP, DNO, Neptune Energy and Spirit Energy through a Joint Industry Project on Fault-controlled Deposits.

Appendix A. Supplementary data

Supplementary data to this article can be found online at https://doi.org/10.1016/j.marpetgeo.2020.104614.

References

Aase, N.E., Walderhaug, O., 2005. The effect of hydrocarbons on quartz cementation: diagenesis in the upper Jurassic sandstones of the Miller field, North Sea, Revisited. Petrol. Geosci. 11 (3), 215–223.

Bernabé, Y., Li, M., Maineult, A., 2010. Permeability and pore connectivity: a new model based on network simulations. J. Geophys. Res.: Solid Earth 115 (10), 1–14.

Bertei, A., Nicolella, C., 2011. Percolation theory in SOFC composite electrodes: effects of porosity and particle size distribution on effective properties. J. Power Sources 196 (22), 9429–9436. https://doi.org/10.1016/j.jpowsour.2011.06.087.

Bjørlykke, K., Nedkvitne, T., Ramm, M., Saigal, G.C., 1992. Diagenetic processes in the brent group (middle Jurassic) reservoirs of the North Sea: an overview. Geol. Soc. Lond. Spec. Publ. 61 (1), 263–287.

Bourbié, T., Zinszner, B., 1985. Hydraulic and acoustic properties as a function of porosity in Fontainebleau sandstone. J. Geophys. Res. B B13, 11524–11532.

Buades, A., Coll, B., Morel, J.-M., 2008. Nonlocal image and movie denoising. Int. J. Comput. Vis. 76 (2), 123–139. https://doi.org/10.1007/s11263-007-0052-1.

Buades, a., Coll, B., Morel, J.M., 2010. Image denoising methods. A new nonlocal principle. SIAM Rev. 52 (1), 113–147.

Bultreys, T., Stappen, J.V., Kock, T.D., Boever, W.D., Boone, M.A., Hoorebeke, L.V., Cnudde, V., 2016. Investigating the relative permeability behavior of microporosity-rich carbonates and tight sandstones with multiscale pore network models. J. Geophys. Res.: Solid Earth 121 (11), 7929–7945.

Chiarella, D, Capella, W, Longhitano, S.G, Muto, F, 2020. Fault-controlled base-of-scarp deposits. Basin Research. In press.

Doyen, P.M., 1988. Permeability, conductivity, and pore geometry of sandstone. J. Geophys. Res. 93 (B7), 7729 http://doi.wiley.com/10.1029/JB093iB07p07729.

Giles, M., Stevenson, S., Martin, S., Cannon, S., Hamilton, P., Marshall, J., Samways, G., 1992. The reservoir properties and diagenesis of the brent group: a regional perspective. Geol. Soc. Lond. Spec. Publ. 61 (1), 289–327.

Gomez, C.T., Dvorkin, J., Vanorio, T., 2010. Laboratory measurements of porosity, permeability, resistivity, and velocity on Fontainebleau sandstones. Geophysics 75 (6), E191.

Iassonov, P., Gebrenegus, T., Tuller, M., 2009. Segmentation of X-ray computed tomography images of porous materials: a crucial step for characterization and quantitative analysis of pore structures. Water Resour. Res. 45 (9).

Ketcham, R.A., Carlson, W.D., 2001. Acquisition, optimization and interpretation of X-ray computed tomographic imagery: applications to the geosciences. Comput. Geosci.

Lindquist, W.B., Venkatarangan, A., Dunsmuir, J., Wong, T.-f., 2000. Pore and throat size distributions measured from synchrotron X-ray tomographic images of Fontainebleau sandstones. J. Geophys. Res.: Solid Earth 105 (B9), 21509–21527. https://agupubs.onlinelibrary.wiley.com/doi/abs/10.1029/2000JB900208.

Lu, J., Wilkinson, M., Haszeldine, R.S., Boyce, A.J., 2011. Carbonate cements in Miller field of the UK North Sea: a natural analog for mineral trapping in CO2 geological storage. Environ. Earth Sci. 62 (3), 507–517.

Maast, T.E., Jahren, J., Bjørlykke, K., 2011. Diagenetic controls on reservoir quality in middle to upper Jurassic sandstones in the South Viking graben, North Sea diagenetic controls on reservoir quality in the South Viking graben sandstones. AAPG Bull. 95 (11), 1883–1905.

Madonna, C., Quintal, B., Frehner, M., Almqvist, B.S.G., Tisato, N., Pistone, M., Marone, F., Saenger, E.H., 2013. Synchrotron-based X-ray tomographic microscopy for rock physics investigations. Geophysics 78 (1), D53–D64. http://library.seg.org/doi/abs/10.1190/geo2012-0113.1.

Marchand, A.M., Haszeldine, R.S., Smalley, P.C., Macaulay, C.I., Fallick, A.E., 2001. Evidence for reduced quartz-cementation rates in oil-filled sandstones. Geology 29 (10), 915–918.

Marcussen, Ø., Maast, T.E., Mondol, N.H., Jahren, J., Bjørlykke, K., 2010. 'Changes in physical properties of a reservoir sandstone as a function of burial depth–the etive formation, northern North Sea'. Mar. Petrol. Geol. 27 (8), 1725–1735.

Mavko, G., Nur, A., 1997. The effect of a percolation threshold in the Kozeny-Carman relation, Gary Mavko and Amos Nur. Geophysics 62 (5), 1480–1482.

McClure, N., Brown, A., 1992. Miller Field: A Subtle Upper Jurassic Submarine Fan Trap in the South Viking Graben, United Kingdom Sector, North Sea: Chapter 20'.

Mehmani, A., Milliken, K., Prodanović, M., 2019. Predicting flow properties in diagenetically-altered media with multi-scale process-based modeling: a Wilcox formation case study. Mar. Petrol. Geol. 100, 179–194.

Mehmani, A., Prodanović, M., 2014. The effect of microporosity on transport properties in porous media. Adv. Water Resour. 63, 104–119.

Otsu, N., 1979. A threshold selection method from gray-level histograms. IEEE Trans. Syst. Man Cybernet. 9 (1), 62–66.

Pal, N.R., Pal, S.K., 1993. A review on image segmentation techniques. Pattern Recogn. 26 (9), 1277–1294.

Revil, A., Kessouri, P., Torres-Verdín, C., 2014. Electrical conductivity, induced polarization, and permeability of the Fontainebleau sandstone. Geophysics 79 (5), D301–D318. http://library.seg.org/doi/abs/10.1190/geo2014-0036.1.

Rooksby, S.K., 1991. The Miller field, blocks 16/7B, 16/8B, UK North Sea. In: United Kingdom Oil and Gas Fields, 25 Years Commemorative Volume, vol. 14, pp. 159–164.

Sezgin, M., Sankur, B., 2004. Survey over image thresholding techniques and quantitative performance evaluation. J. Electron. Imag. 13 (1), 146–166.

Soulaine, C., Gjetvaj, F., Garing, C., Roman, S., Russian, A., Gouze, P., Tchelepi, H.A., 2016. The impact of sub-resolution porosity of X-ray microtomography images on the permeability. Transport Porous Media 113 (1), 227–243.

Thomson, P.-R., Aituar-Zhakupova, A., Hier-Majumder, S., 2018. Image segmentation and analysis of pore network geometry in two natural sandstones. Front. Earth Sci. 6 (June), 1–14. https://www.frontiersin.org/articles/10.3389/feart.2018.00058/full.

Thomson, P.-R., Ellis, R., Chiarella, D., Hier-Majumder, S., 2020. Microstructural analysis from X-ray CT images of the Brae formation sandstone, North Sea. Front. Earth Sci. 8, 246. https://doi.org/10.3389/feart.2020.00246.

Thomson, P.-R., Hazel, A., Hier-Majumder, S., 2019. The influence of microporous cements on the pore network geometry of natural sedimentary rocks. Front. Earth Sci. 7, 48. https://www.frontiersin.org/article/10.3389/feart.2019.00048.

Trier, Ø.D., Jain, A.K., 1995. Goal-directed evaluation of binarization methods. IEEE Trans. Pattern Anal. Mach. Intell. (12), 1191–1201.

Turner, C.C., Cronin, B.T., 2018. The Brae Play, South Viking Graben, North Sea; An Introduction.

van de Lagemaat, J., Benkstein, K., Frank, A., 2001. Relation between particle coordination number and porosity in nanoparticle films: implications to dye-sensitized solar cells. J. Phys. Chem. B 105 (50), 12433–12436.

Wildenschild, D., Vaz, C., Rivers, M., Rikard, D., Christensen, B., 2002. Using X-ray computed tomography in hydrology: systems, resolutions, and limitations. J. Hydrol. 267 (3–4), 285–297.

Wimert, J.T., Hier-Majumder, S., 2012. 'A three-dimensional microgeodynamic model of melt geometry in the earth's deep interior'. J. Geophys. Res. Solid Earth 117 (B04), B04203.

Youssef, S., Rosenberg, E., Gland, N., Kenter, J., Skalinski, M., Vizika, O., 2007. High resolution CT and pore-network models to assess petrophyscial properties of homogeneous and heterogeneous carbonates. In: PE/EAGE Reservoir Characterization and Simulation Conference, p. 12.

Zou, R., Bian, X., Pinson, D., Yang, R., Yu, A., Zulli, P., 2003. Coordination number of ternary mixtures of spheres. Particle & Particle Systems Characterization20(5), 335–341. In: 4th World Congress on Particle Technology (WCPT4), Sydney, Australia, July 21-25, 2002.